Frontiers in Bioscience Landmark

Front. Biosci. (Landmark Ed) **2022**; 27(1): 015
http://doi.org/10.31083/j.fbl2701015

Original Research

The structural aspects of neural dynamics and information flow

JunHyuk Woo[1,2], Kiri Choi[3], Soon Ho Kim[1], Kyungreem Han[1,*], MooYoung Choi[2,*]

[1]Laboratory of Computational Neurophysics, Convergence Research Center for Brain Science, Brain Science Institute, Korea Institute of Science and Technology, 02792 Seoul, Republic of Korea
[2]Department of Physics and Astronomy and Center for Theoretical Physics, Seoul National University, 08826 Seoul, Republic of Korea
[3]School of Computational Sciences, Korea Institute for Advanced Study, 02455 Seoul, Republic of Korea
*Correspondence: khan@kist.re.kr (Kyungreem Han); mychoi@snu.ac.kr (MooYoung Choi)
Academic Editor: Igor Lavrov
Submitted: 11 October 2021 Revised: 6 December 2021 Accepted: 27 December 2021 Published: 12 January 2022

Abstract

Background: Neurons have specialized structures that facilitate information transfer using electrical and chemical signals. Within the perspective of neural computation, the neuronal structure is an important prerequisite for the versatile computational capabilities of neurons resulting from the integration of diverse synaptic input patterns, complex interactions among the passive and active dendritic local currents, and the interplay between dendrite and soma to generate action potential output. For this, characterization of the relationship between the structure and neuronal spike dynamics could provide essential information about the cellular-level mechanism supporting neural computations. **Results**: This work describes simulations and an information-theoretic analysis to investigate how specific neuronal structure affects neural dynamics and information processing. Correlation analysis on the Allen Cell Types Database reveals biologically relevant structural features that determine neural dynamics—eight highly correlated structural features are selected as the primary set for characterizing neuronal structures. These features are used to characterize biophysically realistic multi-compartment mathematical models for primary neurons in the direct and indirect hippocampal pathways consisting of the pyramidal cells of Cornu Ammonis 1 (CA1) and CA3 and the granule cell in the dentate gyrus (DG). Simulations reveal that the dynamics of these neurons vary depending on their specialized structures and are highly sensitive to structural modifications. Information-theoretic analysis confirms that structural factors are critical for versatile neural information processing at a single-cell and a neural circuit level; not only basic AND/OR but also linearly non-separable XOR functions can be explained within the information-theoretic framework. **Conclusions**: Providing quantitative information on the relationship between the structure and the dynamics/information flow of neurons, this work would help us understand the design and coding principles of biological neurons and may be beneficial for designing biologically plausible neuron models for artificial intelligence (AI) systems.

Keywords: Neuronal structure; Neural dynamics; Neural information; Information-theoretic analysis; Direct/indirect hippocampal pathways

1. Introduction

Neurons are classified structurally according to the branching patterns of their dendrites and axons: a multipolar neuron has several dendrites and an axon, a bipolar neuron contains a dendrite and an axon, a pseudo-unipolar neuron has an axon that splits into two branches, and a unipolar neuron possesses only a single axon [1]. The multipolar neurons constitute the most prevalent type in the vertebrate central nervous system and are regarded as responsible for high-order computations while bipolar and pseudo-unipolar neurons play important roles in the sensory system. Unipolar neurons have only a limited role for vertebrates, although they are the dominant type in invertebrates.

Even for the same type of neurons in the same region of the brain, the dendritic structures of neurons are diverse [2–7], leading to different dynamics of action potentials [8–10]. Neurons whose dendritic structures consist of many branches [8] with a high degree of asymmetry [9] tend to generate high-frequency regular spikes or burst-firing. Neurons whose apical dendrites are either too large or too small are less likely to burst upon either somatic or dendritic stimulation [10]. Subcellular structures are also strongly correlated with neuronal dynamics. For example, spines, which are tiny and highly motile membrane protrusions, are the primary structure for synapse formation that greatly affects neural dynamics and computations. They are morphologically classified into filopodia, thin, stubby, mushroom, and branched types, each exhibiting different physicochemical properties [11,12]. Rich dynamics in creation, type-transition, translocation, and clustering of spines would influence the synaptic transmission and learning. The axon initial segment (AIS), the proximal portion of the axon beginning at the emergence of the axon from the soma (the axon hillock) and ending at the onset of the myelin sheath, is responsible for initiating action potentials [13]. Moreover, changes in structural properties of AIS (which usually occurs in time scales of hours to days [14]) fine-tune the spiking behavior of neurons: if the AIS locates distally from the soma, the somatic voltage threshold [15,16] and the width of the action potential decrease [16].

Table 1. Structural features of neurons.

Feature	Name	Description
S_1	Average local bifurcation angle	The average angle between the first two compartments (in degree) at a bifurcation.
S_2	Average contraction	The average ratio between the Euclidean distance of a branch and its path length. Euclidean distance of a branch represents the straight-line distance from the soma to the branch. The path length is given by the sum of the lengths between each node along the path.
S_3	Average diameter	The average diameter of all compartments of the neuron.
S_4	Average parent-daughter ratio	The average ratio between the diameter of a daughter branch and its parent branch. One value for each daughter branch is generated at each bifurcation point.
S_5	Maximum branch order	The maximum order of the branch. The order of a branch is defined with respect to the soma of which the branch order vanishes. The first bifurcation has a branch order equal to unity, the second bifurcation has a branch order two, and so on.
S_6	Maximum Euclidean distance to root	The maximum Euclidean distance of all nodes. Euclidean distance corresponds to the straight line distance from the soma (root) to the node.
S_7	Maximum path distance to root	The maximum path distance of all nodes. The path distance is the sum of lengths of all connected nodes from the soma, ending with that node.
S_8	Number of bifurcations	The number of bifurcations for the neuron. A bifurcation point has two daughters.
S_9	Number of branches	The number of branches in the neuron. A branch consists of one or more compartments that lie between two branching points or between one branching point and a termination point.
S_{10}	Number of nodes	The total number of nodes in the given input neuron. A node represents a single sample point of the neuron defined by its coordinates, a radius, and its connectivity to other nodes in the neuron.
S_{11}	Number of stems	The number of stems attached to the soma. Except for the node designating the soma, each node is labeled as a stem.
S_{12}	Number of tips	The number of terminal tips for the given input neuron. This function counts the number of nodes that are terminal endpoints.
S_{13}	Soma surface area	The surface area of the soma is computed by one of two methods. If the soma is composed of just one node then the sphere assumption is used; otherwise, the sum of external cylindrical surfaces of nodes forming the soma is calculated.
S_{14}	Total length	The total length of a neuron is computed as the sum of distances between two connected nodes for all branches of the input neuron.
S_{15}	Total surface area	The total surface area of the entire neuron.
S_{16}	Total volume	The total volume of the entire neuron.

The strategies for neuron modeling are diverse, ranging from simple integrate-and-fire (IF) modeling [17–19], Hodgkin-Huxley type biophysical modeling [20,21], to multi-compartmental biophysical approaches [22,23]. The multi-compartmental models are of primary importance for characterizing neural dynamics and computation because the models can reproduce both spatial and temporal behaviors of neurons. Moreover, the model structure can be highly realistic via three-dimensional morphological reconstruction of biological neurons [23]. Ever since the pioneering work of Warren S. McCulloch and Walter Pitts in 1943 [24], developing biologically plausible neuron models for artificial neural networks and neuromorphic systems has attracted the computational neuroscience community. While simple neuron models can be easily implemented in artificial neural networks or neuromorphic systems [25], they are incapable of modeling properly the rich dynamics of the dendrite, axon, and subcellular structures that are important for neural computations [26–28]. In this context, the ideal treatment would be to start from biophysically realistic multi-compartment models and to reduce the models, with the intrinsic dynamics and computational capabilities of biological neurons retained, which are then implementable in artificial intelligence (AI) systems [25,29].

This study explores how the structural properties of neurons affect neural dynamics and information processing. We first analyze the Allen Cell Types Database [30] to understand correlations between structural features and electrophysiological properties of biological neurons. Based on the knowledge of biological neurons, the dynamics and coding properties of biophysically realistic multi-compartment models for three primary neurons in the direct and indirect hippocampal pathways are systemically investigated.

By way of outline, Section 2 (Methods) describes structural and electrophysiological features of neurons (2.1), multi-compartmental neuron models (2.2), and the

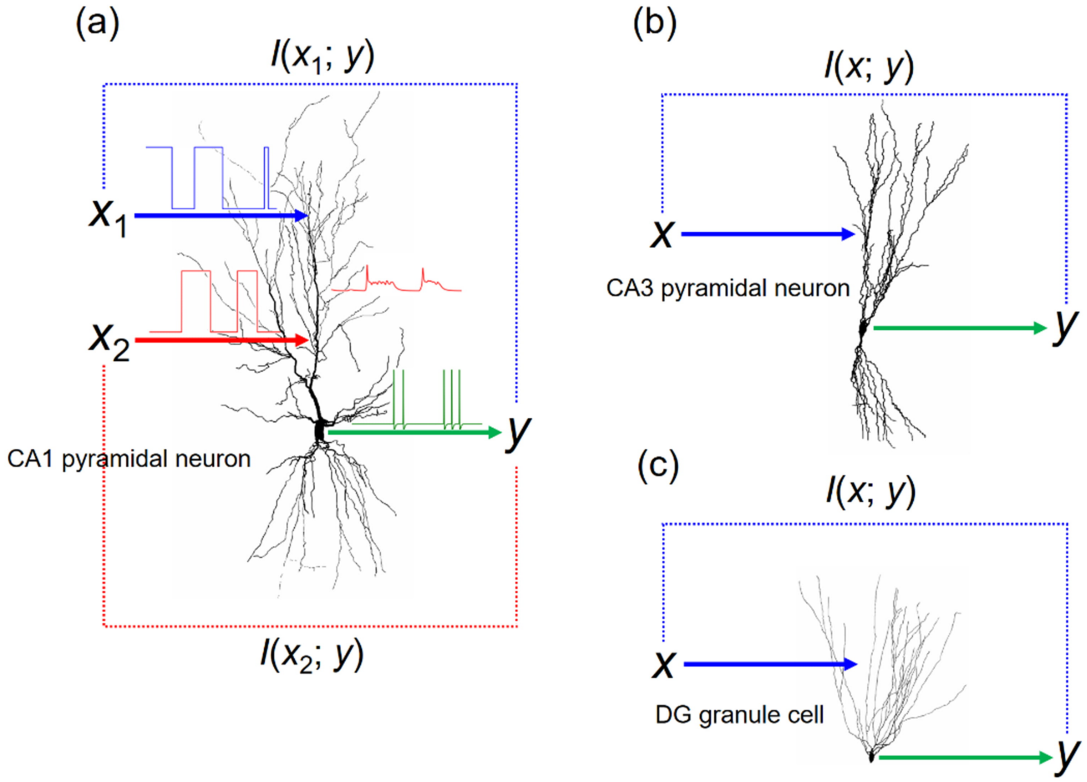

Fig. 1. An information-theoretic framework for evaluating neural information processing of models for hippocampal neurons. (a) Illustration for the CA1 pyramidal neuron. Two synaptic inputs (blue and red arrows) are presented on the apical dendrite. The synaptic inputs are triggered by hidden states x_1 and x_2, with coherence α between them. The output spike train is measured at the soma (green arrow). Exemplary patterns of the hidden state and output spike train are displayed above the corresponding arrows; that of the excitatory postsynaptic potential (EPSP) in the upper right (red curve). Mutual information $I(x_i, y)$ between x_i (i = 1 or 2) and output y is calculated. Schematics for the (b) CA3 pyramidal neuron and (c) DG granule cell.

information-theoretic framework for evaluating neural information processing (2.3). Section 3 (Results) begins with the correlation analysis of the Allen Cell Types Database, which helps identify relevant structural features for determining electrophysiological properties (3.1), characterizes the effects of structural modifications on neuronal dynamics and computation at a single-cell level (3.2), and describes the structural effects on the neural circuit behavior (3.3). Section 4 combines Discussion and Conclusions.

2. Methods

2.1 Structural and electrophysiological features of neurons

We use most of the structural and electrophysiological features introduced in the Allen Cell Types Database [30] to characterize both biological neurons and neuron models. Table 1 lists the structural attributes and their definitions. In the Allen Cell Types Database, the structural attributes (S_1 to S_{16}) are defined based on the detailed cell morphology obtained via tissue sections *in situ* and reconstructions of individual neurons [31]. The electrophysiological features are based on information about spiking behaviors obtained from whole-cell patch-clamp recordings with three types of stimulus protocols, including long square current, ramp current, and short square current injections [32]. The electrophysiological features are classified into the spike train-related features (ET_1 to ET_4) and spike shape-related features (ES_1 to ES_{36}), as summarized in **Supplementary Table 1** in supplementary material.

2.2 Multi-compartment neuron models

The neuron models for three primary cells in the hippocampus, i.e., the pyramidal cell in Cornu Ammonis 1 (CA1), that in CA3, and granule cell in the dentate gyrus (DG), are systemically analyzed (Fig. 1). These models were developed by Vetter *et al.* (ModelDB accession 7907) [33] to examine the effects of dendrite structures on the efficacy of the forward/backward propagation of action potentials; the models describe realistic structures via three-dimensional morphological reconstruction of biological neurons [34–36]. All dendrites are divided into compartments with a maximum length of 7 mm. Two Hodgkin–Huxley-type conductances (g_{Na} and g_K) are inserted into the soma and dendrites at uniform densities. The model is tuned by attaching a synthetic axon. The uniform pas-

sive parameters of the model are R_i = 150 Ω·cm, C_m = 1 μF/cm^2, and R_m = 12 kΩ·cm^2. The standard values for g_{Na} and g_K are 35 and 30 pS/mm^2, respectively. Channel kinetics and densities are adjusted at temperature 37 °C.

The synaptic conductance is described in terms of the dynamics of ionotropic glutamate receptors such as the α-amino-3-hydroxy-5-methyl-4-isoxazole propionic acid (AMPA) receptor, based on the work by Vetter *et al.* [33]. The dynamic behaviors of receptors are fitted with biexponential function with the exponential rise and decay time constants of 0.2 and 1.7 ms, respectively; a reversal potential of the conductance is set to 0 mV and a maximum synaptic conductance to 50 nS. This allows obtaining the time evolution of the receptor conductance to evaluate the information processing at the synapse level.

We modify the three primary structural factors (i.e., dendritic length, diameter, and the number of branches) to test if these factors can influence neural dynamics and information processing. The lengths or diameters of all dendritic compartments in the model are multiplied by the same value (e.g., 2-fold increase or 0.5-fold decrease). The number of branches is varied in the following manner: either new branches with fixed diameter and length (e.g., 0.5 μm in diameter and 156 μm in length) are added to the bifurcation sites (i.e., nodes of a parent branch segment where the branch is divided into two daughter branches) of the parent branches, or the shorter branches on the randomly chosen bifurcation sites are deleted. All simulations have been performed via the NEURON program (v7.8, https://neuron.yale.edu/) [37,38] with a time step of 0.01 ms.

2.3 Information-theoretic framework

Mutual information between a presynaptic binary hidden state and the axonal output spike train provides a useful tool for characterizing neural information processing of the neuron models. We extend the information-theoretic framework, first suggested by Denève and colleagues [39–43], to include multiple synapses and hidden states, similarly to our previous work [44]. The binary hidden state of a neuron represents a stimulus that appears and disappears randomly. For instance, the stimulus may correspond to a bar with a given orientation in a visual receptive field or a sound with a preferred frequency. Each of the hidden states x_1 and x_2 takes the value 1 or 0 for the state on or off, respectively. The coherence between x_1 and x_2 is measured by α in the range [0, 1]: α vanishes for the two states behaving independently while it is set equal to unity for the two fully synchronized.

The binary hidden states follow a Markov process with the composite hidden state (x_1, x_2) that changes according to the transition probability $p(x_1x_2 \to x'_1x'_2)$ from (x_1, x_2) to (x'_1, x'_2):

$$
\begin{aligned}
&p(00 \to 00) = (1 - p_{\text{on}})^2 + (p_{\text{on}} - p_{\text{on}}^2)\,\alpha,\\
&p(00 \to 01) = p(00 \to 10) = (p_{\text{on}} - p_{\text{on}}^2)\,(1 - \alpha),\\
&p(00 \to 11) = p_{\text{on}}^2 + (p_{\text{on}} - p_{\text{on}}^2)\,\alpha,\\
&p(01 \to 00) = p(10 \to 00) = (1 - p_{\text{on}})\,p_{\text{off}},\\
&p(01 \to 01) = p(10 \to 10) = (1 - p_{\text{on}})\,(1 - p_{\text{off}}),\\
&p(01 \to 10) = p(10 \to 01) = p_{\text{on}}\,p_{\text{off}},\\
&p(01 \to 11) = p(10 \to 11) = p_{\text{on}}\,(1 - p_{\text{off}}),\\
&p(11 \to 00) = p_{\text{off}}^2 + (p_{\text{off}} - p_{\text{off}}^2)\,\alpha,\\
&p(11 \to 01) = p(11 \to 10) = (p_{\text{off}} - p_{\text{off}}^2)\,(1 - \alpha),\\
&p(11 \to 11) = (1 - p_{\text{off}})^2 + (p_{\text{off}} - p_{\text{off}}^2)\,\alpha,
\end{aligned}
\tag{1}
$$

where $p_{on} = r_{on}\delta t$ and $p_{off} = r_{off}\delta t$ with the simulation time step δt and rate parameters r_{on} and r_{off}. The synaptic inputs triggered by hidden state x_i follow a Poisson process with rates q_{on} and q_{off} for x_i = 1 and 0, respectively. The postsynaptic spike train $y(t)$ is defined as follows: It takes the value unity (y = 1) or vanishes (y = 0) according to whether or not the membrane potential of the soma crosses 0 mV in the positive direction. For the simulations with a single hidden state x, the transition probability is the marginal distribution of Eqn. 1.

The mutual information $I(x_i; y)$ between the hidden state x_i and the postsynaptic spike train y is given by

$$
I(x_i; y) = H(x_i) - H(x_i \mid y), \tag{2}
$$

where the entropy $H(x_i)$ of x_i is estimated as

$$
H(x_i) = -\langle x_i\rangle \log_2 \langle x_i\rangle - (1 - \langle x_i\rangle) \log_2 (1 - \langle x_i\rangle) \tag{3}
$$

and the conditional entropy

$$
\begin{aligned}
H(x_i \mid y) &= -\langle x_i \log_2 p(x_i = 1 \mid y) + (1 - x_i) \log_2 p(x_i = 0 \mid y)\rangle\\
&= -\langle x_i \log_2 p(x_i = 1 \mid y) + (1 - x_i) \log_2 [1 - p(x_i = 1 \mid y)]\rangle
\end{aligned}
\tag{4}
$$

with angled brackets denoting time averages. The conditional probability $p(x_i \mid y)$ is computed by calculating the posterior log-likelihood of the hidden state being on (x_i = 1), based on the input history:

$$
L_i(t) = \log_2 \frac{p(x_i = 1 \mid y)}{p(x_i = 0 \mid y)}. \tag{5}
$$

We estimate the posterior log-likelihood L_i via the differential equation:

$$
\frac{\mathrm{d}L_i}{\mathrm{d}t} = r_{\text{on}}(1 + \exp[-L_i]) - r_{\text{off}}(1 + \exp[L_i]) + w\delta[y(t) - 1] + \theta \tag{6}
$$

where $w \equiv \log(f_{on,i}/f_{off,i})$ and $\theta \equiv f_{on,i} - f_{off,i}$ with the mean postsynaptic firing rates $f_{on,i}$ and $f_{off,i}$ for x_i = 1

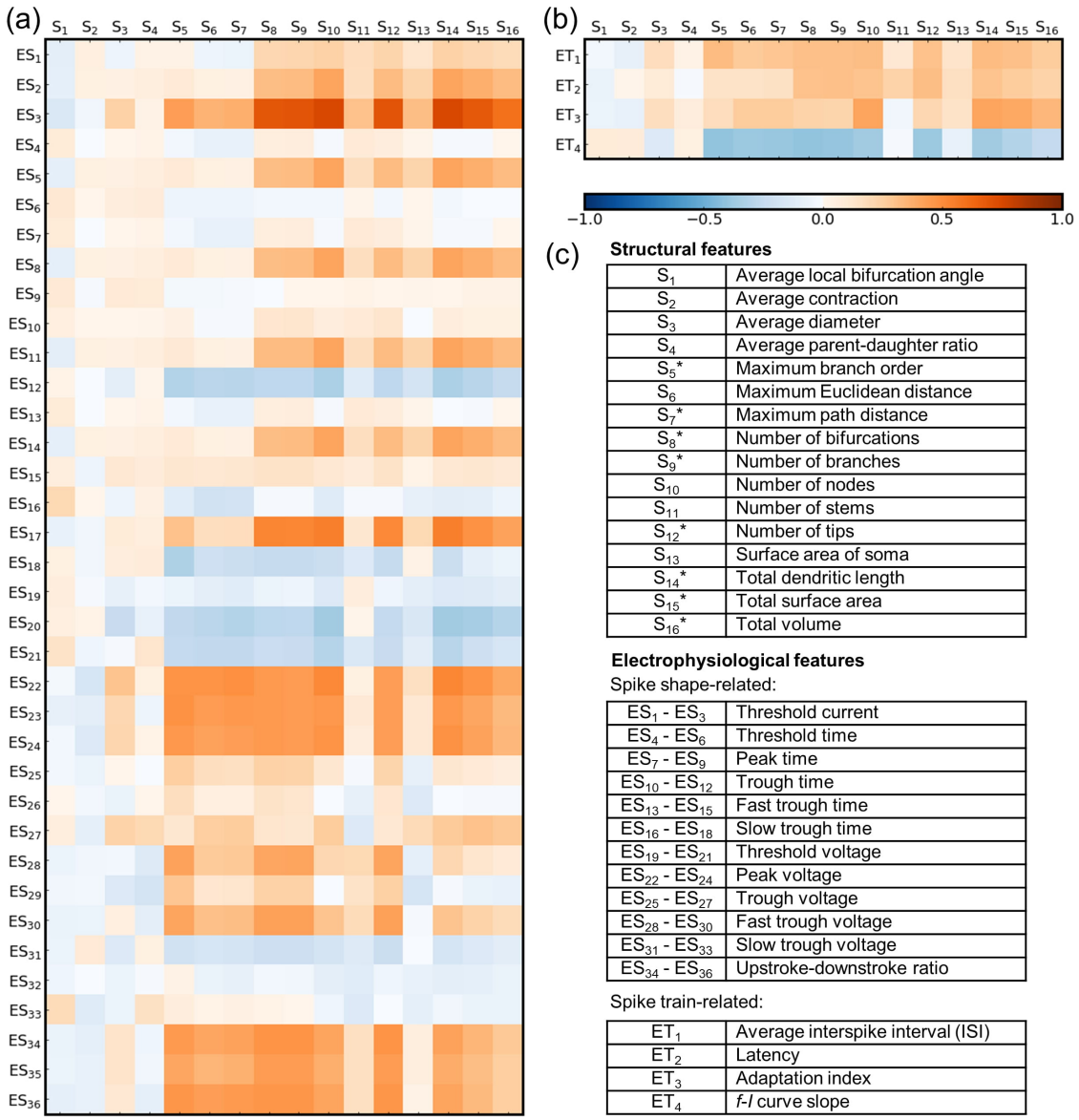

Fig. 2. Correlations between the structural and electrophysiological features of biological neurons in the Allen Cell Types Database. (a) Pearson correlation coefficients between structural features (S_1 to S_{16}) and electrophysiological features regarding spike shape (ES_1 to ES_{36}) and (b) spike train (ET_1 to ET_4). The value and sign of the Pearson correlation coefficient are color-coded; the color scale bar is presented at the bottom of (b). (c) List of structural and electrophysiological features considered in this study. Each of the spike shape-related features has three different values according to the current injection modes. For instance, the 'threshold current' is denoted as ES_1 when the output spike is measured upon a long square current injection, $ES_2$with a ramp injection, and ES_3 for a short square mode. Other spike shape-related features are also displayed in the same order. Eight structural features (S_5, S_7, S_8, S_9, S_{12}, S_{14}, S_{15}, and S_{16}) taken as the primary set to characterize neuron models are marked with asterisks (*). See Table 1 in Methods for detailed descriptions of the structural features and **Supplementary Table 1** in the supplementary material for electrophysiological features.

and 0, respectively. The Dirac delta function $\delta[y(t)-1]$ produces a discontinuous jump when the postsynaptic neuron fires. Eqs. (5) and (6) give $p(x_i=1|\ y)$, which is used for calculating Eq. (4) and thus $I(x_i; y)$.

3. Results

3.1 Correlations between structural and electrophysiological features of biological neurons

Fig. 2 displays Pearson correlation coefficients between the structural and electrophysiological features (i.e., spike shape-related features, denoted as ES_i for $i = 1, \ldots, 36$ and spike train-related ones, ET_i for $i = 1, \ldots, 4$) of biologi-

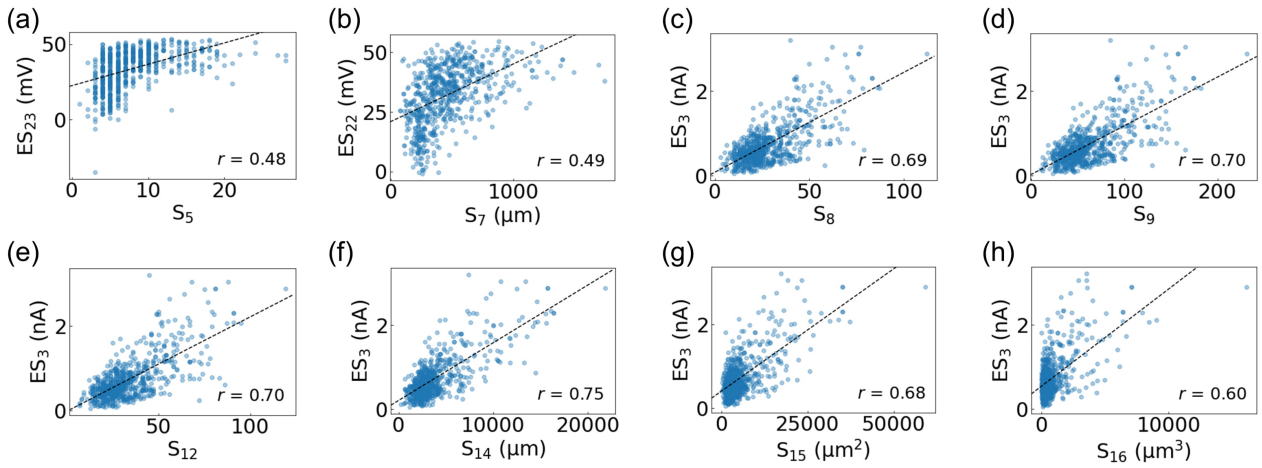

Fig. 3. Correlation analysis of the biological neurons in the Allen Cell Types Database. The most strongly correlated electrophysiological feature for each of the primary structural features is displayed: (a) S_5, (b) S_7, (c) S_8, (d) S_9, (e) S_{12}, (f) S_{14}, (g) S_{15}, and (h) S_{16}. The black dashed line denotes the trend by linear regression and *r* is the Pearson correlation coefficient.

cal neurons in the Allen Cell Types Database. While the average single-neuron structural features, i.e., 'average local bifurcation angle S_1', 'average contraction S_2', 'average diameter S_3', and 'average parent-daughter ratio S_4', are not strongly correlated with either spike shape- or spike train-related features, the non-averaged structural features (S_5 to S_{16}) generally exhibit relatively high positive/negative correlations with the electrophysiological features.

The 'threshold currents (ES_1 to ES_3)' are positively correlated with most of the non-averaged structural features (S_5 to S_{16}). In particular, the correlations are much higher with the short square input currents (with the Pearson correlation coefficients ranging from 0.30 to 0.75 for ES_3), compared with the long square (–0.06 to 0.24 for ES_1) or ramp (0.03 to 0.41 for ES_2) modes (Fig. 2a). Several features such as 'threshold time (ES_5)', 'peak time (ES_8)', 'trough time (ES_{11})', 'fast trough time (ES_{14})', and 'slow trough time (ES_{17})' have positive correlations with the structural features only when the ramp current injection is applied (Fig. 2a). Upon all three injection types (i.e., long square, ramp, and short square modes), 'peak voltages (ES_{22} to ES_{24})' and 'upstroke-downstroke ratios (ES_{34} to ES_{36})' are positively correlated with most of the structural features. In contrast, 'threshold voltages (ES_{19} to ES_{21})' are negatively correlated with the structural features for all the input types. For the spike train-related features, 'average interspike interval (ET_1)', 'latency (ET_2)', and 'adaptation index (ET_3)' are positively correlated with the structural features, but the '*I-f* curve slope (ET_4)' is negatively correlated.

Overall, among the non-averaged features (S_5 to S_{16}), the following features exhibit relatively higher correlations with the above-mentioned electrophysiological features: 'maximum branch order (S_5)', 'maximum Euclidean distance (S_6)', 'maximum path distance (S_7)', 'number of bifurcations (S_8)', 'number of branches (S_9)', 'number of nodes (S_{10})', 'number of tips (S_{12})', 'total dendritic length (S_{14})', 'total surface area (S_{15})' and 'total volume (S_{16})'. However, 'maximum Euclidean distance (S_6)' and 'number of nodes (S_{10})' may not be defined in the multi-compartment neuron models used in the present study. Accordingly, the eight structural features (S_5, S_7, S_8, S_9, S_{12}, S_{14}, S_{15}, and S_{16}, each marked with an asterisk (*) in Fig. 2c) are considered as the primary set for characterizing neuronal structure in most analyses.

Fig. 3 illustrates that the eight primary structural features (i.e., S_5, S_7, S_8, S_9, S_{12}, S_{14}, S_{15}, and S_{16}) are highly correlated with the electrophysiological features. Each panel displays the relationship between each structural feature and its most strongly correlated partner. Most structural features have the highest Pearson correlation coefficient values for ES_3 (i.e., Threshold current to evoke action potentials upon short square input) except S_5 and S_7; S_5 and S_7, which exhibit the highest values with ES_{23} (Peak voltage upon ramp input) and ES_{22} (Peak voltage upon long square input), respectively. The highest Pearson correlation value amounts to 0.75 for the case between S_{14} and ES_3 (Fig. 3f). The full list of Pearson correlation values is presented in **Supplementary Table 2** in the supplementary material.

3.2 Influence of structural change on neuronal dynamics and information processing

The essential dynamic behaviors of the three hippocampal neurons are exhibited in Fig. 4. The long square current input for one second is fed into the soma, and the output spike train at the soma is measured. The *I-f* curve, which represents the relation between firing rate *f* and the magnitude *I* of the input current, is presented in the first

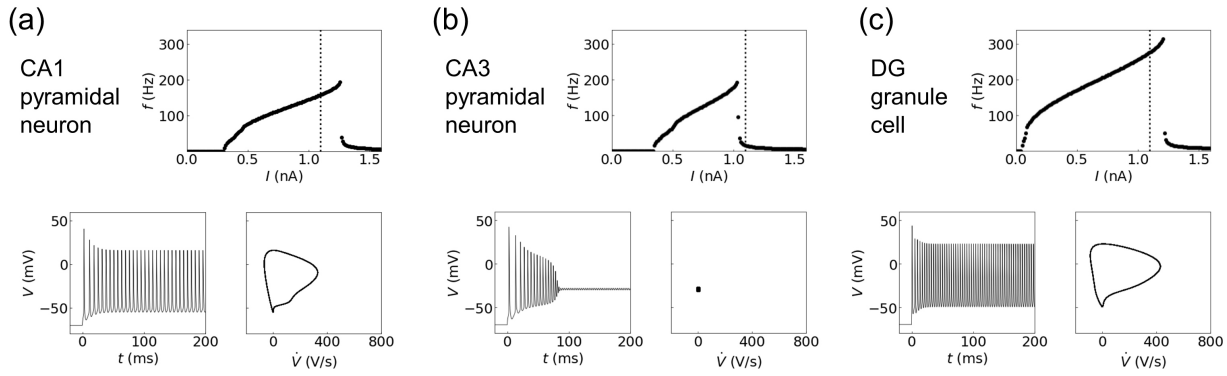

Fig. 4. Dynamics of three hippocampal neurons: (a) pyramidal neuron in CA1 and (b) pyramidal neuron in CA3, and (c) granule cell in the dentate gyrus. The first row displays the *I-f* curves, followed by the time evolution of output spike trains (left) and the phase portraits of steady-state dynamics (100–200 ms) on the $\dot{V}$-V plane (right) in the second row.

row of Fig. 4. The *I-f* relations of CA1 and CA3 pyramidal neurons show similar patterns, with their maximum frequencies around 190 Hz, observed at the input current $I \sim$ 1.26 nA and 1.03 nA for the CA1 neuron and CA3 neuron, respectively. The maximum frequency for the DG granule cell is approximately 315 Hz, much higher than pyramidal neurons. In addition, the rheobase (i.e., the minimum current amplitude that results in an action potential) value for the DG granule cell is much lower than those for the CA1 and CA3 pyramidal neurons.

Upon the input current $I = 1.1$ nA (indicated with vertical dotted line), while the CA1 neuron and DG cell show the regular spiking with a frequency of 158 Hz (for CA1 neuron) and 277 Hz (DG cell), the CA3 neuron manifests bistability at the point called the depolarization block—a silent state that occurs in every neuron when it receives excessive excitation [45]. These dynamical changes of the spike train are captured by the phase portrait of membrane potential V and its time derivative $\dot{V} \equiv \mathrm{d}V/\mathrm{d}t$ (right panel in the second row of Fig. 4). At $I = 1.1$ nA, the limit cycle attractors of CA1 neuron and DG cell reflect their regular spiking behaviors with intrinsic frequencies; CA3 neuron is at the point of transition from the regular spiking to the silent state as represented by a fixed point.

Fig. 5 exhibits how structural modifications affect neural dynamics of the CA1 pyramidal neuron. The resulting neural dynamics upon the structural modifications exhibit reasonable operations. The first column of each row displays the modified structure, followed by the characterization of the structure using the primary features (S_5, S_7, S_8, S_9, S_{12}, S_{14}, S_{15}, S_{16}) of the Allen Cell Types Database (see Table 1 and Fig. 2c); the changes are presented relative to the default values before structural modifications, indicated as $S_i^{(0)}$ for i = 5, 7, 8, 9, 12, 14, 15, and 16 (i.e., fold increase or decrease with respect to the default value, $S_i/S_i^{(0)}$). The last two columns display the *I-f* curve and phase portrait on the V-$\dot{V}$ plane. The simulation condition has been taken the same as in Fig. 4: the output spike train is obtained at the soma upon the long square current input for one second.

When the dendritic lengths are increased by 2-fold from the total basal dendritic length of 15.76 mm (Fig. 5a), two directly related structural features 'maximum path distance (S_7)' and 'total dendritic length (S_{14})' are doubled; 'total surface area (S_{15})' and 'total volume (S_{16})' exhibit ~2-fold increases. The *I-f* curve (the third column) moves to the right, indicating that the rheobase and the threshold current for depolarization block become higher. At a given input current (e.g., $I = 0.4$ nA, marked with the vertical dotted line), the neuronal firing is reduced compared to the dynamics of the original model (the green curve). In contrast, when dendritic lengths are decreased in half (i.e., $S_{14}/S_{14}^{(0)} = 0.5$), its *I-f* curve is shifted to the left, indicating that the modified model can fire under smaller input currents (i.e., lower rheobase) than the normal model (Fig. 5b). The threshold current for the depolarization block is also lower than the default value. The shapes and sizes of the limit cycles of the modified structures are significantly changed from that of the normal structure (the last column of Fig. 5); this implies that the meaningful change in the spiking behavior occurs upon the modification of dendritic length.

We now compare the results of varying the dendritic lengths with those from modifications of the number of dendritic branches. Dendritic branches are added to make the total dendritic length double (**Supplementary Fig. 1a** in Supplementary material): a branch (156.07 μm in length, 0.5 μm in diameter) is added to each of all 101 bifurcation points, leading to a total increase of about 15.76 mm. In accord, five features related directly to the modification, 'maximum branch order (S_5)', 'number of bifurcations (S_8)', 'number of branches (S_9)', 'number of tips (S_{12})', and 'total dendritic length (S_{14})' are doubled (i.e., $S_i/S_i^{(0)} \approx 2$ for i = 5, 8, 9, 12, and 14) (the second column of **Supplementary Fig. 1a**). Dendritic branches are randomly

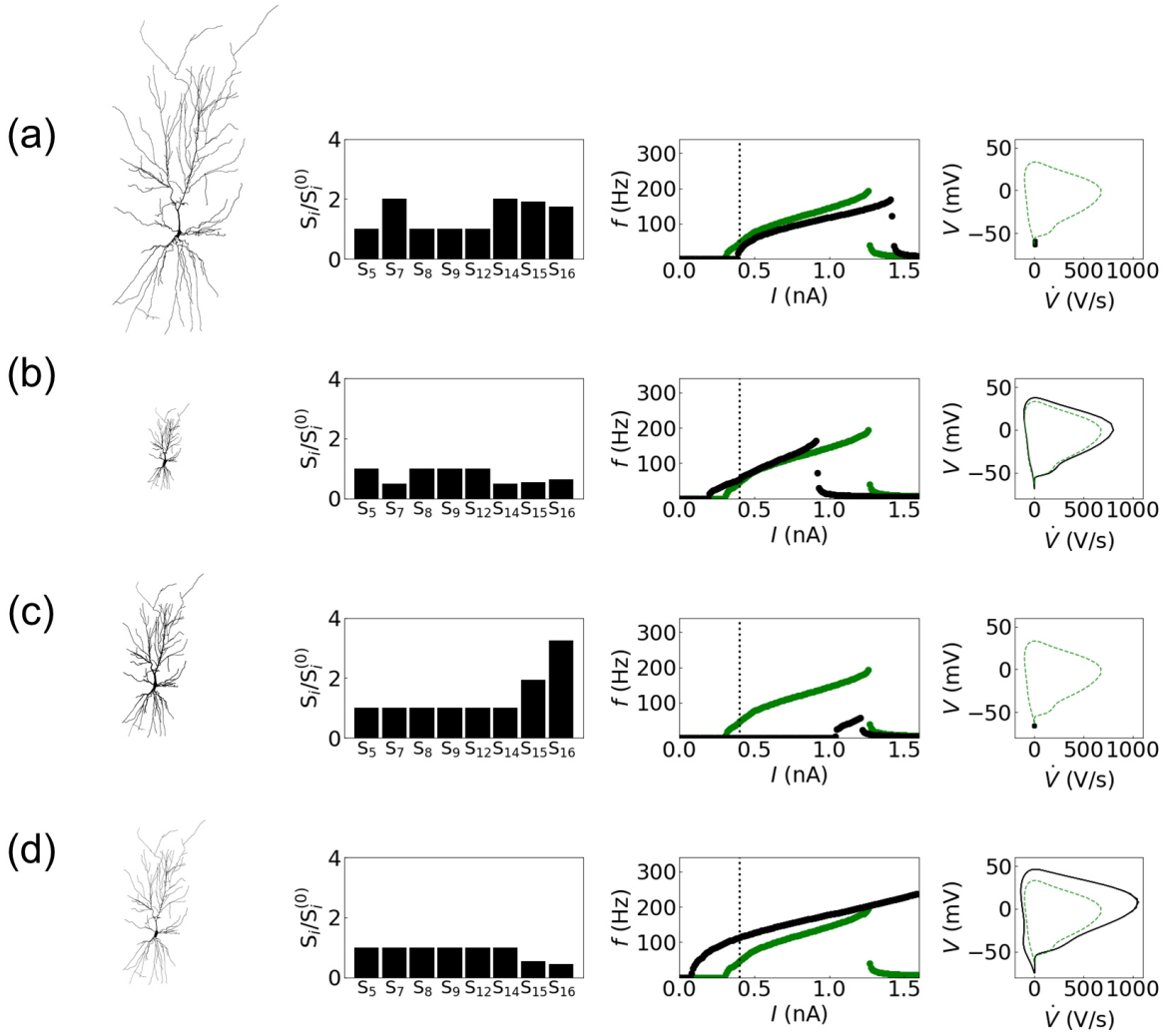

Fig. 5. Influence of structural changes in the CA1 pyramidal neuron dynamics: (a) 2-fold increase and (b) 0.5-fold decrease in the dendritic length, and (c) 2-fold increase and (d) 0.5-fold decrease in the dendritic diameter. The first column displays the modified model structures, followed by the characterization of modified structures using the primary structural features of the Allen Cell Types Database (the second column) and the *I-f* curves (the third column). The *I-f* curves of the original structure and of the modified structure are plotted in green and in black, respectively. The last column exhibits the phase portrait on the V-$\dot{V}$ plane at $I = 0.4$ nA. The black solid line/dot and the green dashed line represent the results with and without structural changes, respectively.

removed to reduce the total dendritic length in half (i.e., $S_{14}/S_{14}^{(0)} \approx 0.5$). When the number of dendrites is increased by 2-fold, the *I-f* curve moves to the right (**Supplementary Fig. 1a**), whereas upon removing the dendritic branch the operation range is extended (i.e., the rheobase is decreased and the threshold for depolarization block is increased) (**Supplementary Fig. 1b**). Although the total dendritic length change is the same as the corresponding modifications of dendritic lengths without adding or removing any branches (Fig. 5a and 5b), the shapes of *I-f* curves are significantly different between each of the corresponding conditions (Fig. 5a and 5b): the model with 2-fold increased dendritic length (Fig. 5a) exhibits a larger operation range, exhibiting a lower rheobase and a higher threshold current for depolarization block. The model with a 0.5-fold decreased dendritic length (Fig. 5b) has a similar rheobase value as the case of deleting branches (**Supplementary Fig. 1b**), but the threshold current for depolarization block is much lower. It is revealed that the dendritic diameter also has a significant influence on the spike dynamics as captured by the *I-f* curve. Unlike previous structural modifications, increasing the diameter by 2-fold significantly lowers the maximum frequency of firing to ~ 57 Hz (Fig. 5c), and decreasing the diameter by 0.5-fold (Fig. 5d) promotes the maximum frequency to ~ 237 Hz (at $I = 1.6$ nA). Again, the phase portraits on the V-$\dot{V}$ plane manifest significantly different output spike trains between the different structural modifications. The shapes of action potentials are not changed notably upon all the structural variations (data not shown).

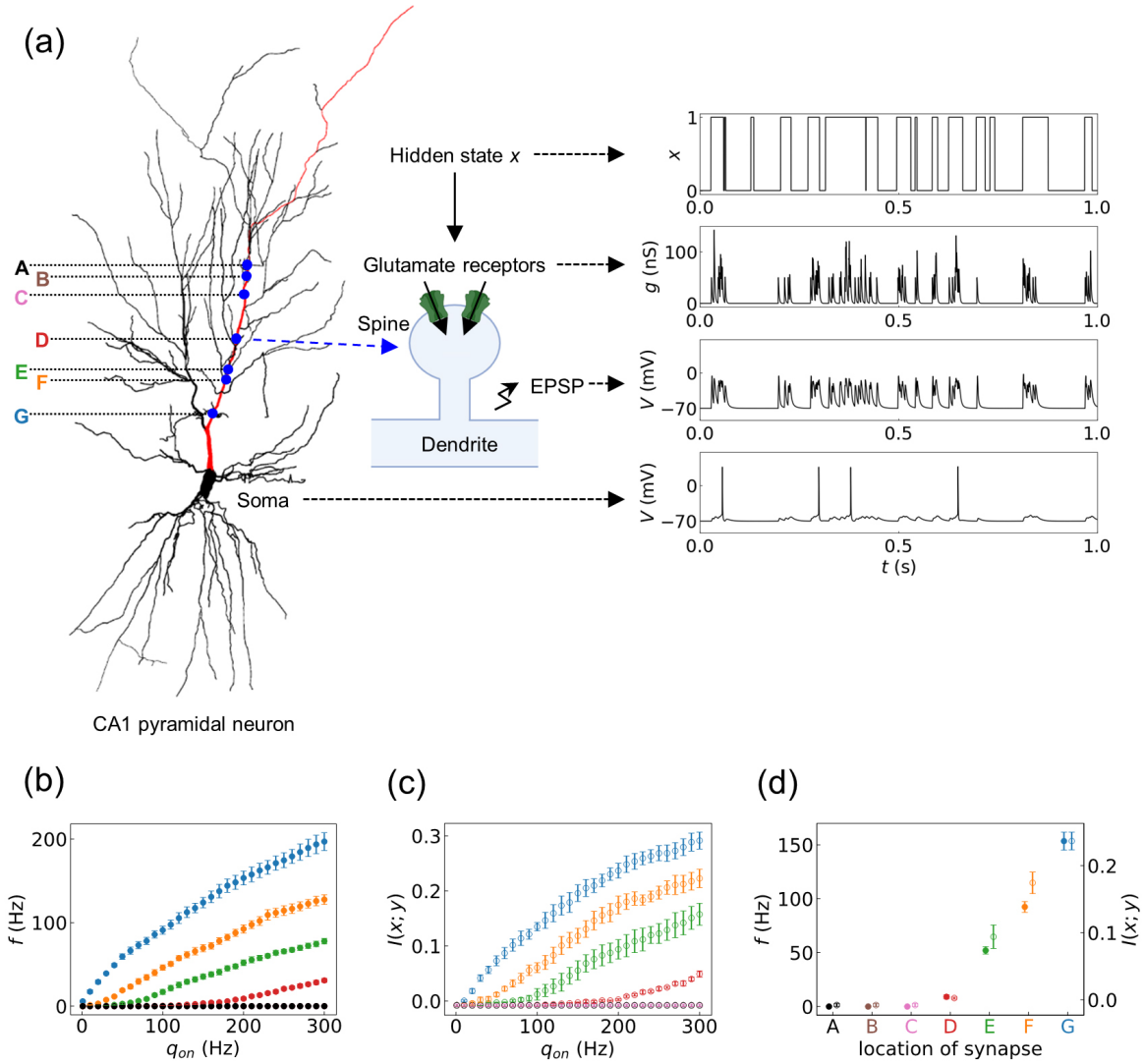

Fig. 6. Effects of stimulus location on dynamics and information processing of the CA1 pyramidal neuron. (a) Schematic diagram of information transfer in the neuron. The path that we focused on the dendritic tree is colored in red and the locations of the synaptic input (i.e., A to G) are marked with blue dots. The dynamics of the neuron when the synapse is placed on D is shown on the right. Synaptic input triggered by the hidden state x is transmitted through the AMPA-type glutamate receptors on the spine. The stimulation changes the conductance of the receptors, which in turn evokes the excitatory postsynaptic potential (EPSP). The EPSP is propagated down from the dendrite to soma. Mutual information $I(x; y)$ between hidden state x and spike train y at the soma is quantified. (b) Dependence of postsynaptic firing rate f on presynaptic firing rate q_{on} for each location of synaptic input (i.e., A–G). The circles are colored according to the location of the stimulus as follows: black denotes location A; brown, B; pink, C; red, D; green, E; orange, F; blue, G. Error bars indicate standard error of five independent simulations. Circles for locations A–C overlap at all points. (c) Dependence of mutual information $I(x; y)$ on q_{on}. (d) Dependence of f and $I(x; y)$ on the location of the stimulus when q_{on} = 200 Hz. Filled and empty circles indicate f and $I(x; y)$, respectively. In (b) and (c), circles representing frequencies and mutual information upon the stimuli at locations A, B, C overlap each other; their values are all zero because no action potentials are generated.

The detailed dynamics and information processing of the CA1 pyramidal neuron model are displayed in Fig. 6. The schematic diagram in Fig. 6a illustrates the information transfer pathway in the neuron. The hidden state triggers a synaptic input that stimulates the AMPA-type glutamate receptors of a synapse located on a dendritic spine. The resulting EPSP travels from the dendrite to the soma. The mutual information $I(x; y)$ quantifies the total information transmitted from the hidden state to the postsynaptic spike train. The presynaptic stimulus is provided on a synapse at one of seven equidistant locations on an apical dendrite branch labeled A–G; the seven locations are 50 μm apart with distances ranging from 100 (A) to 400 μm (G) from the soma along the dendritic branch in three-dimensional

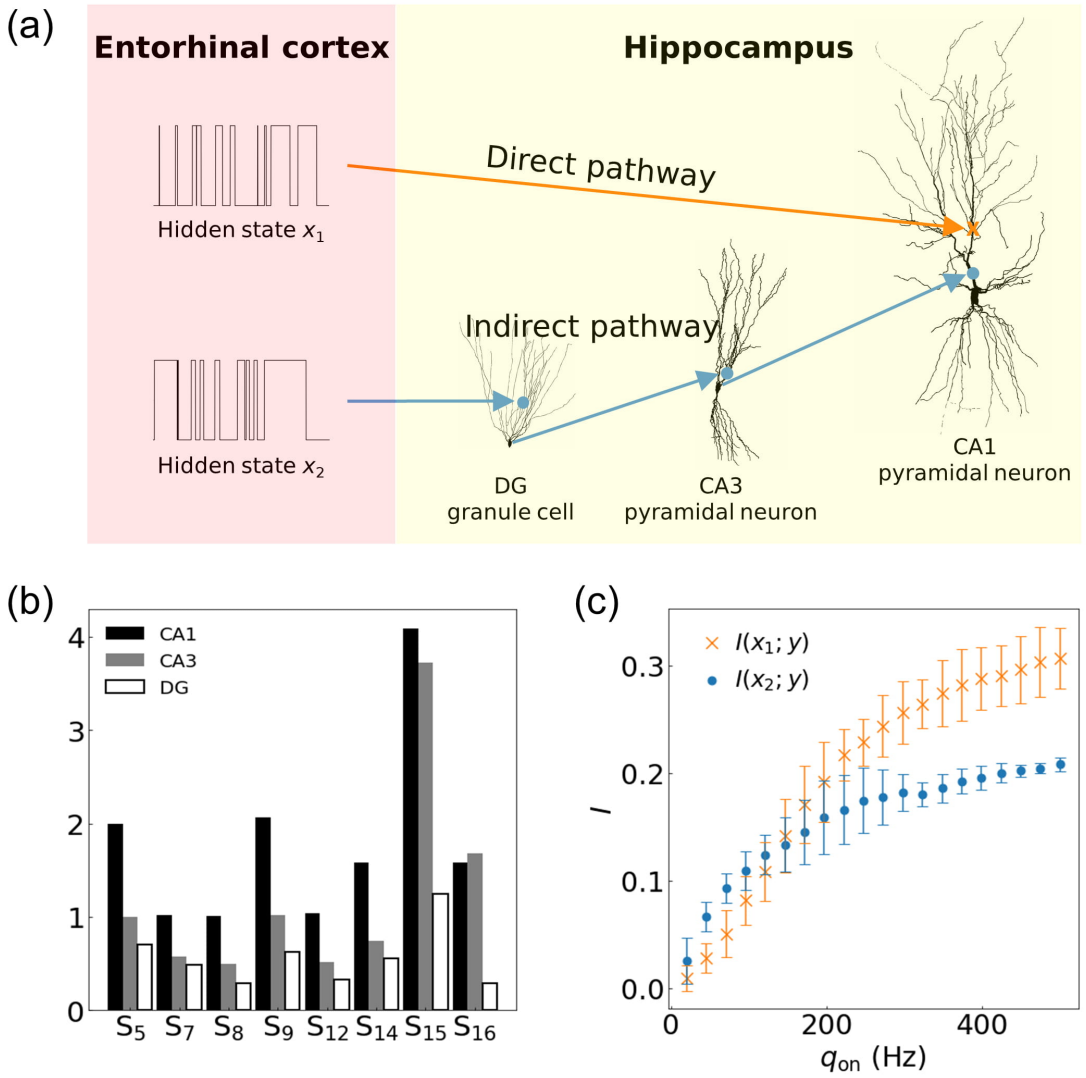

Fig. 7. Characterizations of the hippocampal direct and indirect pathways. (a) Schematic diagram of the circuit constructed using pyramidal neurons in CA1 and CA3, and a granule cell in DG. Two hidden states x_1 and x_2, coupled with a coherence $\alpha = 0.1$, trigger synaptic inputs from the entorhinal cortex to the hippocampal neurons. The input triggered by x_1 stimulates a distal synapse located on the dendrite of the CA1 pyramidal neuron and the input triggered by x_2 stimulates the DG granule cell, which transmits the signal to the CA3 pyramidal neuron; this in turn stimulates a proximal synapse on the dendrite of CA1 pyramidal neuron. (b) Primary structural features (see Fig. 2) of the neurons in the circuit. Black, gray and white colors indicate the CA1 pyramidal neuron, CA3 pyramidal neuron, and DG granule cell, respectively. Each structural feature has its own unit: S_5, 10^1; S_7, 10^3 μm; S_8, 10^2; S_9, 10^2; S_{12}, 10^2; S_{14}, 10^4 μm; S_{15}, 10^4 μm^2 and S_{16}, 10^4 μm^3. (c) The effect of presynaptic firing rate $q_{on,i}$ on the mutual information $I(x_i; y)$ between the hidden state x_i and the output y of the CA1 pyramidal neuron. Orange crosses indicate mutual information of the direct pathway $I(x_1; y)$ as a function of $q_{on,1}$ with $q_{on,2}$ fixed to 1 Hz, while blue filled circles denote the mutual information of the indirect pathway $I(x_2; y)$ as a function of $q_{on,2}$ with fixed to 1 Hz. Error bars represent the standard deviations of five independent simulations.

space. On the right of Fig. 6a, the time evolutions of the hidden state, the conductance of the AMPA-type glutamate receptor, EPSP, and the membrane potential of the soma are shown when the presynaptic stimulus is provided at location D.

Fig. 6b and 6c display the firing rate and mutual information of the CA1 pyramidal neuron upon varying presynaptic firing rate q_{on}. The minimum q_{on} required for firing (i.e., threshold) is much lower for proximal locations such as G and F than for distal ones. The threshold values increase nonlinearly with the distance from the soma. Both the firing rate and mutual information increase in a roughly linear manner once the threshold is reached. Fig. 6d plots the postsynaptic firing rate and mutual information for varying stimulus locations at q_{on} = 200 Hz: there are no neural activity and information transfer when the presynaptic in-

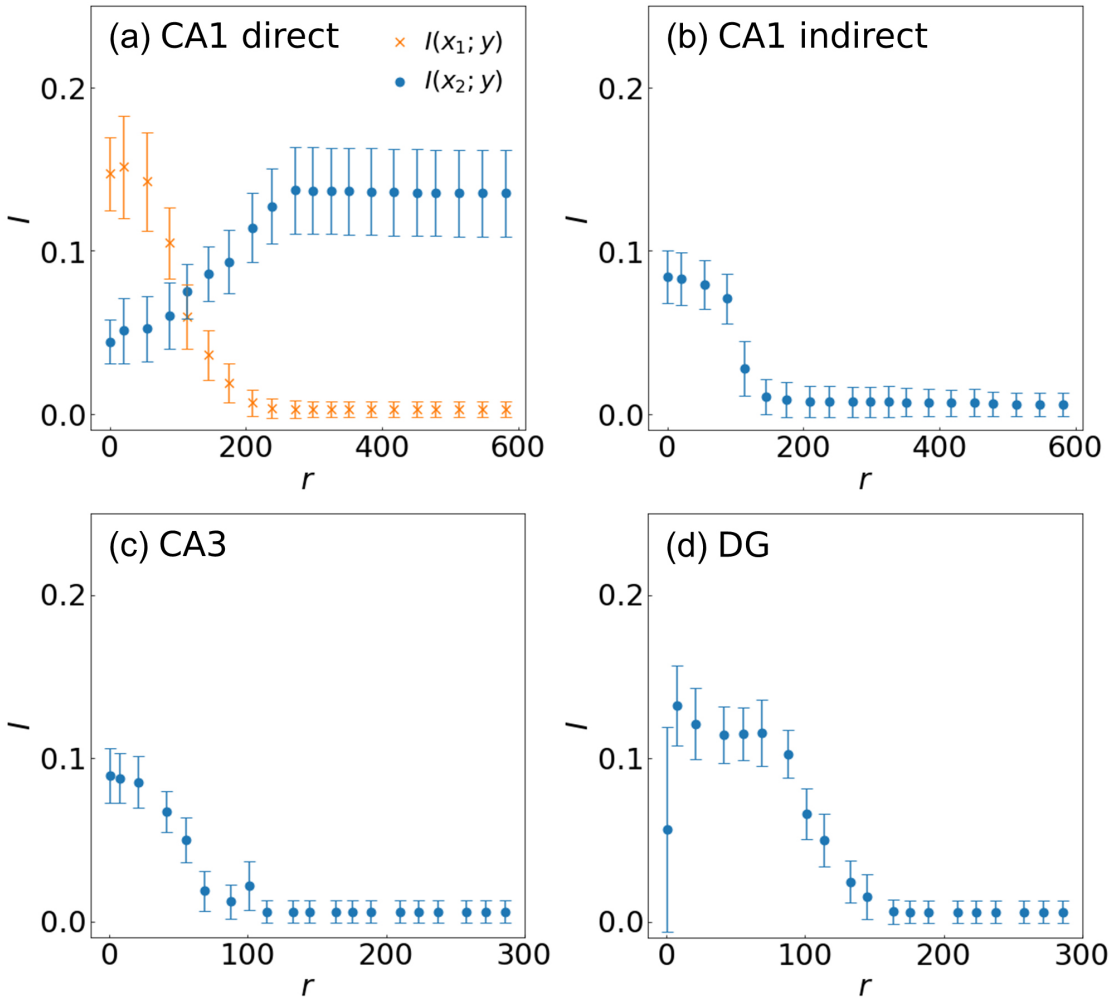

Fig. 8. Information processing of the hippocampal pathways depending on the location of synapses in the (a) CA1 pyramidal neuron receiving input from the direct pathway and (b) indirect pathway, (c) CA3 pyramidal neuron, and (d) DG granule cell. The coloring and symbols are the same as in Fig. 7. The location of the synapse is expressed as the path distance r from the soma. Firing rates $q_{on,i}$ (i = 1 or 2) are set to be 150 Hz. Error bars indicate standard errors for five independent simulations.

puts are provided at locations A to C. In contrast, the dynamics and information transfer drastically increase as the input location is moved further toward G.

The information processing of the CA1 pyramidal neuron shown in Fig. 6 can be mapped to AND/OR-like Boolean operations depending on the synaptic location. When the stimulus is given proximal to the soma (e.g., G), a low q_{on} is sufficient to evoke the postsynaptic neuronal activity and the information transfer—this can be mapped to an OR logic gate in which only one 'true' input is necessary for 'true' output. For distal locations (D or E), a higher q_{on} is required for the neuronal activity/information transfer, which corresponds to an AND gate that needs more than one 'true' input for 'true' output. At locations A to C, the synapse is insufficient to transfer information by itself and cannot be mapped to a logic operation within the observed q_{on} values (0–300 Hz).

3.3 Structural effects on the hippocampal pathways

Based on the single-cell level information, we analyze the information processing of the direct and indirect hippocampal pathways consisting of CA1, CA3, and DG cells. This circuit is a computational representation of the biological two-input system of CA1 [46–48], where the CA1 pyramidal neuron can take inputs either directly or indirectly. This circuit is the primary information processing unit for match/mismatch calculation between what is encountered and what is expected—this continuous calculation is important for memory encoding and retrieval in the hippocampus [49–51]. Hidden state x_1 of the entorhinal cortex initiates the direct pathway of the circuit, where the input triggered by x_1 is delivered to a distal region of the CA1 dendrite.

Hidden state x_2 is a part of the indirect pathway, whereby the input propagates from DG, through CA3, to a proximal region of CA1 (Fig. 7a). Two hidden states x_1 and x_2 are coupled with the coherence α, which is set equal to 0.1.

The structural properties of the three neurons in the circuit are characterized using the eight primary structural features obtained from the Allen Cell Types Database (Fig. 7b). Most of the features are the largest for the CA1 pyramidal neuron and the smallest for the DG granule cell. However, total volume (S_{16}) is the largest for the CA3 pyramidal neuron, followed by the CA1 pyramidal neuron and the DG granule cell.

The dynamic ranges of mutual information of the two pathways for the firing rate are compared in Fig. 7c. Overall, both mutual information increase with the firing rate: the mutual information of the indirect pathway is higher than that of the direct pathway under a relatively lower firing rate (i.e., $q_{on} <$ ~120 Hz), whereas they are reversed at higher firing conditions. This result from circuit analysis can be applied to optimal circuit control, as the input control is usually the most accessible parameter to modify. For example, let us consider the goal to ensure a similar level of information transfer from both the direct and indirect pathways; then the correct choice would be around $I(x_1, y) = I(x_2, y) = 0.2$, $q_{on,1} \sim 200$ Hz and $q_{on,2} \sim 500$ Hz.

Variations of information flow upon change of the location of synapses have been systemically examined. The location of a synapse is varied while keeping the others at the initial location (Fig. 8)—the dendritic length and dendritic diameters are fixed, while both the direct and indirect pathways are activated at the same time ($q_{on,1} = 150/q_{on,2} = 150$). For each condition, we calculate the mutual information $I(x_i, y)$ between x_i ($i = 1$ or 2) and the output y. The mutual information increases as the synapses are located closer (proximal) to the soma, but up to an extent. The signal gets saturated, where the mutual information starts to drop afterward. We have observed a similar trend when pushing other variables to induce a stronger response. One interesting observation we make is on the proximal synapse of the CA1 pyramidal neuron, where the signal from the indirect pathway is overwhelmed by the signal from the direct pathway when the proximal synapse is too close to the soma. The locations of two synapses to CA1 have considerable influence on the overall operation of the circuit and must be finely tuned such that none of the pathways dominate the output. The structural features of each neuron can also be tuned to maximize the difference between the mutual information when only one of the pathways is turned on. For the ideal operation of the circuit, the location of two synapses must be placed optimally, which can be inferred from Fig. 8.

We then explore how the modification of neuronal structure can control the information processing of the direct and indirect hippocampal pathways. The mutual information increases with shorter dendritic length (L) and smaller dendritic diameter (D) (Fig. 9). Again, the primary structural features are used for describing these structural modifications. Modifying L or D has similar structural effects for all three neuron types. Four structural features, S_7, S_{14}, S_{15}, and S_{16}, have a linear relationship with L. As D increases, S_{15} also increases linearly, while the increase of S_{16} is proportional to D^2. Here, either direct or indirect pathway is activated (i.e., $q_{on,1} = 150/q_{on2} = 1$ or $q_{on,1} = 1/q_{on,2} = 150$) to characterize the information processing of each pathway. In the CA1 pyramidal neuron, which is the only neuron in the circuit in the direct pathway, structural features (S_7, S_{14}, S_{15}, and S_{16} for length modification; S_{15} and S_{16} for diameter modification) are negatively correlated with $I(x_1; y)$. For the indirect pathway, $I(x_2; y)$ remains unchanged by the length modification in CA1 and CA3 pyramidal neurons. When the diameter is modified, $I(x_2; y)$ shows the inverted sigmoidal shape. Exceeding certain values of S_{15} and/or S_{16} might induce a rapid decrease in $I(x_2; y)$. Structural modifications of the DG granule cell result in a different outcome. As the length of the dendrite is increased, S_7, S_{14}, S_{15}, and S_{16} show negative correlations with $I(x_2; y)$, and diameter modification of the DG granule cell makes no change in $I(x_2; y)$.

We notice that the trend is not universal, as certain parts of the circuit have a very limited impact on controlling the mutual information. This is particularly recognizable when the indirect pathway is activated. Structural features such as the dendritic diameter of DG (D_{DG}), dendritic length of CA3 (L_{CA3}), and dendritic length of CA1 (L_{CA1}) have minimal influence on the mutual information, making these features nonoptimal targets for neural circuit control.

The results under high coherence conditions (i.e., $\alpha = 0.9$) are presented in **Supplementary Fig. 2** in the supplementary material. When two inputs are highly coherent, the profile of the mutual information from the indirect pathway is synchronized strongly to that of the direct pathway. Furthermore, we see a non-negligible basal level of the mutual information regardless of the input status, reducing the overall dynamic range. By comparing the results under low and high coherence conditions, we identify conditions that can be mapped to the specific Boolean logic operations. The OR operation is trivial as the CA1 neuron can transfer signals from either direct or indirect pathway and both at the same time, as long as the circuit is configured to process signals through each pathway. The AND operation emerges when signals from individual pathways are configured to be weak (e.g., both synapses to CA1 are too distal or the dendritic length and diameter are too large), but the synchronized input from both pathways starts to recover I. We also notice the possibility of the XOR-like operation by controlling the firing rate under low coherence conditions. When firing rates q_{on} from both pathways are high, the signal can get saturated and I starts to drop; this XOR-like nature may contribute to the intrinsic computational capability of the circuit, that is mismatch/match calculations for memory encoding/retrieval [49–51].

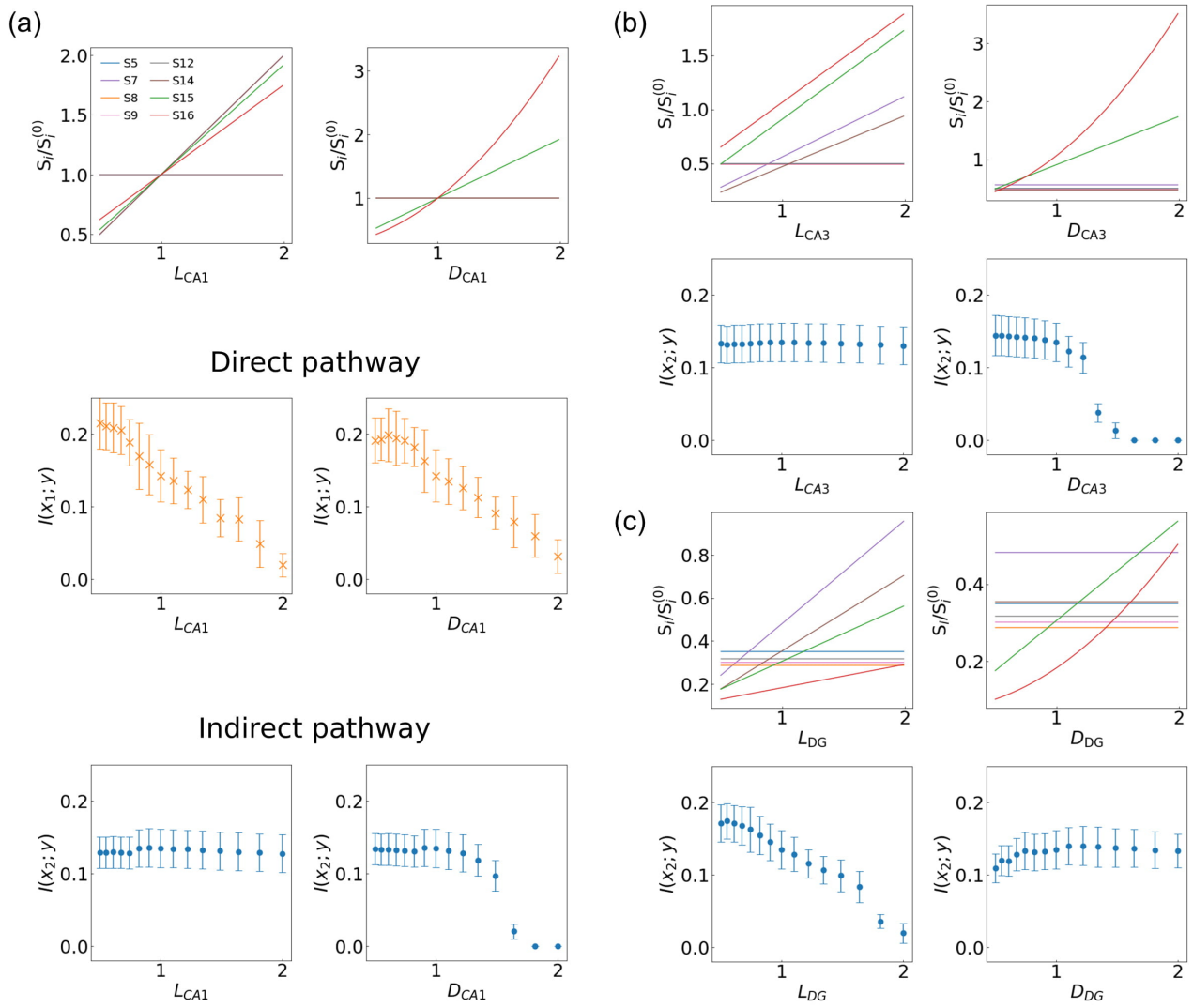

Fig. 9. Influence of structural changes of the (a) CA1 pyramidal neuron, (b) CA3 pyramidal neuron, and (c) DG granule cell on the information processing of direct and indirect hippocampal pathways. Left and right columns indicate the modification in length L_R and diameter D_R of the corresponding neuron (Subscript R denotes CA1, CA3, or DG). The top panels of each subfigure represent the eight primary structural features (see Fig. 2) changed by the structural modification. In the remaining figures, mutual information $I(x_1; y)$ between hidden state x_1 and output y of the CA1 pyramidal neuron is marked with orange crosses and $I(x_2; y)$ with blue-filled circles. For the simulation of $I(x_1; y)$ or $I(x_2; y)$, firing rates ($q_{on,1}$, $q_{on,2}$) have been taken to be (150 Hz, 1 Hz) or (1 Hz, 150 Hz). Standard errors have been calculated in five independent simulations.

4. Discussion and conclusions

This study has investigated the structural aspects of neural dynamics and computations via computer simulations and information-theoretic analysis. Beginning with an exploration of the Allen Cell Types Database [30] to obtain the correlations between structural and electrophysiological features of biological neurons, we have systemically investigated the neuronal dynamics through biophysically realistic multi-compartment mathematical models. The three primary cells in the hippocampus (two pyramidal neurons, one in the CA1 region and the other in the CA3 region, and a granule cell of the dentate gyrus) have been chosen for the computational analysis. These neurons are adequate for characterizing the relationship between neural dynamics and underlying structural mechanisms at both the single-neuron scale and their interactions: the neurons not only have intrinsic dynamical and coding properties rooted in their structures but also contribute to mismatch/match detection via the direct/indirect hippocampal pathways [51–54]. Although their computational properties have attracted the interest of both theoreticians and experimentalists, detailed dynamics and mechanisms underlying their compu-

tational capabilities remain to be clarified. The analysis has been extended with information-theoretic methods to characterize how neuronal structure affects Boolean logic operations at the single-cell level and higher-level computations through the hippocampal pathways.

The Allen Cell Types Database is a large unique dataset containing quantitative structural and electrophysiological features measured via the standardized procedure. In the database, structural features (S_1 to S_{16}) are described based on the cell morphology information from tissue sections *in situ* and that from reconstructions of individual neurons. In addition, electrophysiological features, i.e., spike shape-related (ES_1 to ES_{36}) and spike train-related features (ET_1 to ET_4), have been defined according to the cell firing properties obtained from whole-cell patch-clamp recordings. Both structural and electrophysiological features are necessary for inferring the correlations between the structural features and neural dynamics that are usually expressed in terms of electrophysiological properties (Fig. 2). The selected structural features exhibiting high correlations with the electrophysiological features have been used for characterizing biophysically realistic multi-compartment neuron models for the three primary hippocampal neurons. In consequence, ten biologically relevant structural features for neuronal dynamics have been obtained: 'maximum branch order (S_5)', 'maximum Euclidean distance (S_6)', 'maximum path distance (S_7)', 'number of bifurcations (S_8)', 'number of branches (S_9)', 'number of nodes (S_{10})', 'number of tips (S_{12})', 'total dendritic length (S_{14})', 'total surface area (S_{15})' and 'total volume (S_{16})'. Then eight features out of the ten have been selected: excluded are S_6 and S_{10}, which cannot be properly defined for the neuron models. The eight primary features are highly correlated with electrophysiological features as illustrated in Fig. 3 and **Supplementary Table 2**.

It is manifested that the structural differences among the three primary neurons of the hippocampus lead to large variations in their dynamics. Operation ranges (i.e., the input current between rheobase and the threshold for the depolarization block) and maximum frequencies have turned out to differ significantly, as revealed in the *I-f* profiles (the first row of Fig. 4). In addition, as exhibited by the phase portraits of the output spike trains, their intrinsic spiking behaviors vary according to their unique structures. We have then compared systematically these neurons upon the structural modifications and probed the link between specific structural features and the dynamical properties: the branching patterns have been modified by adding or removing small dendrite branches at bifurcation points, and the dimensions of dendrites have been altered by increasing/decreasing the dendrite length or diameter (Fig. 5). As implied by the modified model structures (the first column of Fig. 5) and the profiles of the structural measures (S_5, S_7, S_8, S_9, S_{12}, S_{14}, S_{15}, S_{16}) (the second column), the neural dynamics varies significantly, depending on the specific structural modifications.

We have also analyzed the more realistic model of a rat neocortical layer 5 pyramidal neuron. The model includes nine ion channels to faithfully reproduce both perisomatic Na^+ and dendritic Ca^{2+} firing behaviors [55], wherein six types of ionic currents (i.e., fast inactivating sodium current, persistent sodium current, muscarinic potassium current, slow inactivating potassium current, fast inactivation potassium current, and fast/non-inactivating potassium current) are uniformly distributed, while three types (i.e., non-specific cation current, high voltage-activated calcium current and low voltage-activated calcium current) are nonuniformly distributed. The effects of structural modifications of length and diameter (**Supplementary Fig. 3**) are in good agreement with the results of the multi-compartment neuron models based on uniform ion channel distributions (Fig. 5). Upon increasing dendritic lengths or diameters, the *I-f* curve of the neocortical layer 5 pyramidal neuron is shifted to the right and the size of the limit cycle on the phase portrait is reduced as in the case of the CA1 pyramidal neuron (Fig. 5); decreasing dendritic lengths or diameters leads to a shift in the *I-f* curve to the left and an increase of the limit cycle size. The characterization of simple neuron models and realistic rodent models provides a starting point for understanding the intrinsic properties of human neocortical neurons. While our understanding of human neurons is often inferred from models based on rodent data, the morphological and biophysical differences between human and rodent neurons may influence neural dynamics and information processing in various ways. The recent development of computational models for human layer 5 cortical neurons by Rich and colleagues lay a foundation for quantitative analysis on the inter-species differences [56].

We have used information theory [57,58] to examine whether the structural modifications of neurons can influence the intrinsic computational abilities of neurons. Ever since the seminal work of MacKay and McCulloch in 1952 [59] that first quantified the information contained in a spike train, numerous measures based on the classical information theory [57] have been devised to quantify information processing in single neurons and between neurons through synaptic transmission. Among these are mutual information which measures the overlapping information between two quantities (e.g., presynaptic input and postsynaptic output) [58], transfer entropy which measures the directionality of information flow [60,61], and partial information decomposition which separates the unique, shared, and synergistic contributions of multiple quantities [62]. We have adopted the method originally proposed by Denève and colleagues [39–43], to measure the mutual information between a hidden state that triggers presynaptic inputs and the postsynaptic output spike trains; this framework provides an ideal means to measure the information processing of a single neuron. Extending this method, we have included two hidden states to characterize the information

processing performed by a neuron receiving inputs from two information sources, which provides a tool to study naturally the hippocampal pathways for mismatch/match calculations via the direct/indirect mutual information flows that can be interpreted as the XOR Boolean logic operations [51–54] (Fig. 9 and **Supplementary Fig. 2**). It has been demonstrated that structural features greatly influence the information processing and logic operation performed at both the single-neuron (i.e., CA1 pyramidal neuron) level (Fig. 5) and the multi-cellular level (Fig. 9 and **Supplementary Fig. 2**).

The quantitative information on the relationship between the structure and the dynamics/computation of neurons may provide a starting point for the in-depth understanding of the design and coding principles of biological neurons. As we have presented evidence here, the structural properties of neurons strongly affect the neural dynamics and information processing—this will eventually guide the cellular-level mechanisms of neural computations including the integration of diverse synaptic input patterns [48,63], complex interactions among the passive and active dendritic local currents [64], and finally the interplay between dendrite and soma for determining the action potential output [8,65–67]. While this computational approach aims to unveil structural aspects of neurons under physiological conditions, the methods can be applied to explore the pathological changes in neurons. For example, in Alzheimer's disease neurons adjacent to amyloid-β (Aβ) plaques are characterized by hyperactivity while neurons in the combined presence of Aβ and tau pathology exhibit hypoactivity [68]; our methods can be used to investigate the mechanisms behind such pathological changes in neural dynamics. Furthermore, this approach may be beneficial for designing biologically plausible neuron models for artificial neural networks and neuromorphic systems.

Abbreviations

AI, artificial intelligence; AIS, axon initial segment; AMPA, α-amino-3-hydroxy-5-methyl-4-isoxazole propionic acid; CA1, Cornu Ammonis 1; CA3, Cornu Ammonis 3; DG, dentate gyrus; IF, integrate-and-fire; EPSP, excitatory postsynaptic potential.

Author contributions

Conceptualization—KH and MYC; modeling and simulations—JHW, KC, SHK, and KH; analysis—JHW, KC, SHK, KH, and MYC; writing—original draft preparation—KH, JHW, and KC; writing—review and editing—KH and MYC; supervision—MYC and KH. All authors have read and agreed to the published version of the manuscript.

Ethics approval and consent to participate

Not applicable.

Acknowledgment

Thanks to all the peer reviewers for their opinions and suggestions.

Funding

This research was funded by Korea Institute of Science and Technology (KIST) Institutional Program (Project No. 2E30951, 2Z06588, and 2K02430) and National R&D Program through the National Research Foundation of Korea (NRF) funded by Ministry of Science and ICT (2021M3F3A2A01037808). KC was supported by the KIAS Individual Grants (Grant No. CG077001). MYC acknowledges the support from the NRF through the Basic Science Research Program (Grant No. 2019R1F1A1046285).

Conflict of interest

The authors declare no conflict of interest.

Supplementary material

Supplementary material associated with this article can be found, in the online version, at https://www.imrpress.com/journal/FBL/27/1/10.31083/j.fbl2701015.

Code availability

All neuron models can be downloaded from the website for ModelDB (https://senselab.med.yale.edu/ModelDB/): Vetter *et al*., accession ID 7907; Hay *et al*., ID 139653. The codes for calculating structural and electrophysiological features are provided by the Allen Cell Types Database (https://celltypes.brain-map.org/); otherwise they are available from the authors upon request (email to khan@kist.re.kr for KH or mychoi@snu.ac.kr for MYC).

References

[1] Kandel ER, Schwartz JH, Jessell TM, Siegelbaum S, Hudspeth AJ, Mack S. Principles of neural science. McGraw-hill: New York, NY. 2000.

[2] Fitch JM, Juraska JM, Washington LW. The dendritic morphology of pyramidal neurons in the rat hippocampal CA3 area. I. Cell types. Brain Research. 1989; 479: 105–114.

[3] Juraska JM, Fitch JM, Washburne DL. The dendritic morphology of pyramidal neurons in the rat hippocampal CA3 area. II. Effects of gender and the environment. Brain Research. 1989; 479: 115–119.

[4] Torben-Nielsen B, Cuntz H. Introduction to Dendritic Morphology. Springer Series in Computational Neuroscience. 2014; 9: 3–22.

[5] Soltesz I. Diversity in the neuronal machine: order and variability in interneuronal microcircuits. Oxford University Press: Oxford. 2006.

[6] Ramaswamy S, Hill SL, King JG, Schürmann F, Wang Y, Markram H. Intrinsic morphological diversity of thick-tufted layer 5 pyramidal neurons ensures robust and invariant properties of in silico synaptic connections. The Journal of Physiology. 2012; 590: 737–752.

[7] Donohue DE, Ascoli GA. A comparative computer simulation

of dendritic morphology. PLoS Computational Biology. 2008; 4: e1000089.
[8] Mainen ZF, Sejnowski TJ. Influence of dendritic structure on firing pattern in model neocortical neurons. Nature. 1996; 382: 363–366.
[9] van Ooyen A, Duijnhouwer J, Remme MWH, van Pelt J. The effect of dendritic topology on firing patterns in model neurons. Network. 2002; 13: 311–325.
[10] van Elburg RAJ, van Ooyen A. Impact of dendritic size and dendritic topology on burst firing in pyramidal cells. PLoS Computational Biology. 2010; 6: e1000781.
[11] Risher WC, Ustunkaya T, Singh Alvarado J, Eroglu C. Rapid Golgi analysis method for efficient and unbiased classification of dendritic spines. PLoS ONE. 2014; 9: e107591.
[12] Berry KP, Nedivi E. Spine Dynamics: are they all the same? Neuron. 2017; 96: 43–55.
[13] Clark BD, Goldberg EM, Rudy B. Electrogenic tuning of the axon initial segment. The Neuroscientist. 2009; 15: 651–668.
[14] Leterrier C. The Axon Initial Segment: an Updated Viewpoint. The Journal of Neuroscience. 2018; 38: 2135–2145.
[15] Goethals S, Brette R. Theoretical relation between axon initial segment geometry and excitability. eLife. 2020; 9: e53432.
[16] Verbist C, Müller MG, Mansvelder HD, Legenstein R, Giugliano M. The location of the axon initial segment affects the bandwidth of spike initiation dynamics. PLoS Computational Biology. 2020; 16: e1008087.
[17] Burkitt AN. A review of the integrate-and-fire neuron model: I. Homogeneous synaptic input. Biological Cybernetics. 2006; 95: 1–19.
[18] Izhikevich EM. Simple model of spiking neurons. IEEE Transactions on Neural Networks. 2013; 14: 1569–1572.
[19] Woo J, Kim SH, Han K, Choi M. Characterization of dynamics and information processing of integrate-and-fire neuron models. Journal of Physics A: Mathematical and Theoretical. 2021; 54: 445601.
[20] Hodgkin AL, Huxley AF. A quantitative description of membrane current and its application to conduction and excitation in nerve. The Journal of Physiology. 2002; 117: 500–544.
[21] Pospischil M, Toledo-Rodriguez M, Monier C, Piwkowska Z, Bal T, Frégnac Y, *et al*. Minimal Hodgkin-Huxley type models for different classes of cortical and thalamic neurons. Biological Cybernetics. 2008; 99: 427–441.
[22] Rall W. Branching dendritic trees and motoneuron membrane resistivity. Experimental Neurology. 1999; 1: 491–527.
[23] Herz AVM, Gollisch T, Machens CK, Jaeger D. Modeling single-neuron dynamics and computations: a balance of detail and abstraction. Science. 2006; 314: 80–85.
[24] McCulloch WS, Pitts W. A logical calculus of the ideas immanent in nervous activity. The Bulletin of Mathematical Biophysics. 1943; 5: 115–133.
[25] Schuman CD, Potok TE, Patton RM, Birdwell JD, Dean ME, Rose GS, *et al.* A Survey of Neuromorphic Computing and Neural Networks in Hardware. arXiv. 2017.
[26] Naud R, Gerstner W. The Performance (and Limits) of Simple Neuron Models: Generalizations of the Leaky Integrate-and-Fire Model. Computational Systems Neurobiology. 2012; 97: 163–192.
[27] Tran-Van-Minh A, Cazé RD, Abrahamsson T, Cathala L, Gutkin BS, DiGregorio DA. Contribution of sublinear and supralinear dendritic integration to neuronal computations. Frontiers in Cellular Neuroscience. 2015; 9: 67.
[28] Brette R, Gerstner W. Adaptive exponential integrate-and-fire model as an effective description of neuronal activity. Journal of Neurophysiology. 2005; 94: 3637–3642.
[29] Indiveri G, Liu S. Memory and Information Processing in Neuromorphic Systems. Proceedings of the IEEE. 2015; 103: 1379–1397.
[30] Allen Institute for Brain Science. Allen Cell Types Database. 2015. Available at: celltypes.brain-map.org (Accessed: 10 October 2021).
[31] Allen Institute for Brain Science. Allen Cell Types Database, Technical White Paper: Morphology. 2018. Available at: celltypes.brain-map.org (Accessed: 10 October 2021).
[32] Allen Institute for Brain Science. Allen Cell Types Database, Technical White Paper: Electrophysiology. 2017. Available at: celltypes.brain-map.org (Accessed: 10 October 2021).
[33] Vetter P, Roth A, Häusser M. Propagation of action potentials in dendrites depends on dendritic morphology. Journal of Neurophysiology. 2001; 85: 926–937.
[34] Li C, Gulledge AT. NMDA Receptors Enhance the Fidelity of Synaptic Integration. Eneuro. 2021; 8: ENEURO.0396–ENEU20.2020.
[35] Hemond P, Migliore M, Ascoli GA, Jaffe DB. The membrane response of hippocampal CA3b pyramidal neurons near rest: Heterogeneity of passive properties and the contribution of hyperpolarization-activated currents. Neuroscience. 2009; 160: 359–370.
[36] Schmidt-Hieber C, Jonas P, Bischofberger J. Subthreshold dendritic signal processing and coincidence detection in dentate gyrus granule cells. The Journal of Neuroscience. 2007; 27: 8430–8441.
[37] Carnevale NT, Hines ML. The NEURON book. Cambridge. 2006.
[38] Hines ML, Carnevale NT. The NEURON simulation environment. Neural Computation. 1997; 9: 1179–1209.
[39] Deneve S. editor Bayesian inference in spiking neurons. Advances in neural information processing systems. MIT Press Cambridge: MA. 2005.
[40] Deneve S. Bayesian spiking neurons I: inference. Neural Computation. 2008; 20: 91–117.
[41] Deneve S. Bayesian spiking neurons II: learning. Neural Computation. 2008; 20: 118–145.
[42] Zeldenrust F, de Knecht S, Wadman WJ, Denève S, Gutkin B. Estimating the Information Extracted by a Single Spiking Neuron from a Continuous Input Time Series. Frontiers in Computational Neuroscience. 2017; 11: 49.
[43] Lochmann T, Denève S. Information transmission with spiking Bayesian neurons. New Journal of Physics. 2008; 10: 55019.
[44] Woo J, Choi K, Kim SH, Han K, Choi M. Characterization of multiscale logic operations in the neural circuits. Frontiers in Bioscience-Landmark. 2021; 26: 723–739.
[45] Bianchi D, Marasco A, Limongiello A, Marchetti C, Marie H, Tirozzi B, *et al*. On the mechanisms underlying the depolarization block in the spiking dynamics of CA1 pyramidal neurons. Journal of Computational Neuroscience. 2012; 33: 207–225.
[46] Venkadesh S, Komendantov AO, Wheeler DW, Hamilton DJ, Ascoli GA. Simple models of quantitative firing phenotypes in hippocampal neurons: Comprehensive coverage of intrinsic diversity. PLoS Computational Biology. 2019; 15: e1007462.
[47] Bezaire MJ, Soltesz I. Quantitative assessment of CA1 local circuits: knowledge base for interneuron-pyramidal cell connectivity. Hippocampus. 2013; 23: 751–785.
[48] Gasparini S, Magee JC. State-dependent dendritic computation in hippocampal CA1 pyramidal neurons. The Journal of Neuroscience. 2006; 26: 2088–2100.
[49] Barrientos SA, Tiznado V. Hippocampal CA1 Subregion as a Context Decoder. The Journal of Neuroscience. 2016; 36: 6602–6604.
[50] Vinogradova OS. Hippocampus as comparator: role of the two input and two output systems of the hippocampus in selection and registration of information. Hippocampus. 2001; 11: 578–598.

[51] Duncan K, Ketz N, Inati SJ, Davachi L. Evidence for area CA1 as a match/mismatch detector: a high-resolution fMRI study of the human hippocampus. Hippocampus. 2012; 22: 389–398.
[52] Vinogradova OS. Hippocampus as comparator: role of the two input and two output systems of the hippocampus in selection and registration of information. Hippocampus. 2001; 11: 578–598.
[53] Kumaran D, Maguire EA. An unexpected sequence of events: mismatch detection in the human hippocampus. PLoS Biology. 2006; 4: e424.
[54] Bezaire MJ, Soltesz I. Quantitative assessment of CA1 local circuits: knowledge base for interneuron-pyramidal cell connectivity. Hippocampus. 2013; 23: 751–785.
[55] Hay E, Hill S, Schürmann F, Markram H, Segev I. Models of neocortical layer 5b pyramidal cells capturing a wide range of dendritic and perisomatic active properties. PLoS Computational Biology. 2011; 7: e1002107.
[56] Rich S, Moradi Chameh H, Sekulic V, Valiante TA, Skinner FK. Modeling Reveals Human–Rodent Differences in H-Current Kinetics Influencing Resonance in Cortical Layer 5 Neurons. Cerebral Cortex. 2021; 31: 845–872.
[57] Shannon CE. A Mathematical Theory of Communication. Bell System Technical Journal. 1948; 27: 623–656.
[58] Stone JV. Principles of Neural Information Theory: Computational Neuroscience and Metabolic Efficiency. Sebtel Press: Sheffield, SYK. 2018.
[59] MacKay DM, McCulloch WS. The limiting information capacity of a neuronal link. The Bulletin of Mathematical Biophysics. 1952; 14: 127–135.
[60] Spinney RE, Prokopenko M, Lizier JT. Transfer entropy in continuous time, with applications to jump and neural spiking processes. Physical Review. E. 2017; 95: 032319.
[61] Schreiber. Measuring information transfer. Physical Review Letters. 2010; 85: 461–464.
[62] Wibral M, Priesemann V, Kay JW, Lizier JT, Phillips WA. Partial information decomposition as a unified approach to the specification of neural goal functions. Brain and Cognition. 2017; 112: 25–38.
[63] Mel BW. Information Processing in Dendritic Trees. Neural Computation. 1994; 6: 1031–1085.
[64] Gidon A, Zolnik TA, Fidzinski P, Bolduan F, Papoutsi A, Poirazi P, *et al*. Dendritic action potentials and computation in human layer 2/3 cortical neurons. Science. 2020; 367: 83–87.
[65] Stuart G, Spruston N, Sakmann B, Häusser M. Action potential initiation and backpropagation in neurons of the mammalian CNS. Trends in Neurosciences. 1997; 20: 125–131.
[66] Williams SR, Stuart GJ. Mechanisms and consequences of action potential burst firing in rat neocortical pyramidal neurons. The Journal of Physiology. 1999; 521: 467–482.
[67] Beaulieu-Laroche L, Toloza EHS, van der Goes M, Lafourcade M, Barnagian D, Williams ZM, *et al*. Enhanced Dendritic Compartmentalization in Human Cortical Neurons. Cell. 2018; 175: 643–651.
[68] Busche MA, Hyman BT. Synergy between amyloid-β and tau in Alzheimer's disease. Nature Neuroscience. 2020; 23: 1183–1193.